

Med-DisSeg: Dispersion-Driven Representation Learning for Fine-Grained Medical Image Segmentation

Zhiquan Chen^{a,b}, Haitao Wang^{a,b}, Guowei Zou^{a,b} and Hejun Wu^{a,b,*}

^aSchool of Computer Science and Engineering, Sun Yat-sen University, Guangzhou, China

^bGuangdong Key Laboratory of Big Data Analysis and Processing, Guangzhou, China

ARTICLE INFO

Keywords:

Medical image segmentation
Representation collapse
Dispersive loss
Attention mechanism
Boundary-aware learning

ABSTRACT

Accurate medical image segmentation is fundamental to precision medicine, yet robust and fine-grained delineation remains challenging under heterogeneous appearances, ambiguous boundaries, and large anatomical variability. In clinical images, targets and surrounding tissues often share similar intensity or texture patterns, which can lead to blurred activations, boundary leakage, and unreliable separation. We attribute these failures to two closely related factors: (i) representation collapse during encoding, where heterogeneous anatomical structures become insufficiently separated in the embedding space, and (ii) inadequate fine-grained multi-scale decoding, where local texture cues and global structural shape are not effectively balanced during reconstruction.

To address these issues, we propose Med-DisSeg, a dispersion-driven medical image segmentation framework that jointly improves representation learning and fine-grained delineation. Med-DisSeg combines a lightweight Dispersive Loss with a task-oriented adaptive attention design for fine-grained anatomical structure segmentation. The Dispersive Loss enlarges inter-sample margins by treating all in-batch hidden representations as negative pairs, yielding well-dispersed and boundary-aware embeddings with negligible overhead. Based on these enhanced representations, the encoder side strengthens structure-sensitive responses through joint channel and spatial modeling, while the decoder side performs multi-scale adaptive calibration to better preserve complementary local-texture and global-shape cues, thereby improving the delineation of small, deformable, and ambiguous structures.

Extensive experiments on five datasets spanning three imaging modalities demonstrate consistent state-of-the-art performance. Moreover, although not specifically tailored for multi-organ CT segmentation, Med-DisSeg achieves competitive results on this benchmark, supporting its robustness and cross-task applicability. **The source code and pretrained models will be released upon acceptance.**

1. Introduction


Medical image segmentation is a cornerstone of precision medicine, supporting lesion detection, organ delineation, pre-operative planning, and treatment evaluation. High-quality segmentation precisely separates targets from background, enabling reliable lesion quantification, radiotherapy planning, and surgical pathway design. As imaging resolutions and clinical workloads continue to increase, there is a growing need for segmentation methods that are both accurate and robust across different anatomies and modalities.

To address these demands, most modern approaches build on U-Net (Ronneberger et al., 2015), which introduced an encoder–decoder architecture with skip connections and established an end-to-end paradigm for medical image segmentation. Subsequent work has mainly improved representation learning and fine-grained delineation within this framework. nnU-Net (Isensee et al., 2021) focuses on self-configuring design and robust engineering to provide strong baseline representations across tasks; Attention U-Net (Oktay et al., 2018) and related variants enhance feature selection along the skip pathways to better highlight lesion regions and boundaries, and more recent Transformer-based or hybrid models, such as TransUNet (Chen et al., 2021)

and UNETR (Hatamizadeh et al., 2022) integrates long-range dependency modeling and global context into U-Net-style encoder–decoder backbones to strengthen high-level representations. In parallel, contrast-driven frameworks such as ConDSeg (Lei et al., 2025) treat medical segmentation as a representation learning problem, encouraging foreground–background separation, and guiding multi-level feature fusion to sharpen object contours.

Despite these gains, two key challenges remain for robust representation learning and fine-grained delineation. First, at the encoding stage, medical image features are prone to feature collapse: heterogeneous structures (e.g., tumors and normal tissues) may be mapped into overly similar embedding spaces, leading to blurred boundaries, reduced segmentation accuracy, and compromised clinical reliability. Second, at the decoding stage, multi-scale fusion and fine-grained focus are often insufficient, especially for small targets and highly deformable structures, limiting the model’s ability to produce precise and clinically reliable predictions.

To address the above challenges in both representation learning and fine-grained delineation, we propose Med-DisSeg, a two-stage medical image segmentation framework in which dispersion regularization and task-oriented adaptive attention operate cooperatively rather than independently.

 wuhejun@mail.sysu.edu.cn (H. Wu)

ORCID(s):

First, Med-DisSeg introduces a Dispersive Loss (DL) that imposes an all-negative constraint among in-batch features. By maximizing the dispersion of hidden embeddings, DL alleviates representation collapse and encourages heterogeneous structures (e.g., lesions and normal tissues) to occupy more separable regions in the feature space, thereby improving discriminability and boundary awareness.

Second, instead of emphasizing standalone module novelty, Med-DisSeg incorporates an adaptive attention mechanism tailored for fine-grained anatomical structure segmentation. At the encoding stage, this mechanism strengthens structure-preserving and boundary-sensitive responses by jointly modeling channel importance and spatial saliency, making feature extraction more robust under heterogeneous appearances and ambiguous boundaries.

Finally, at the decoding stage, Med-DisSeg adopts a multi-scale adaptive calibration strategy to recover subtle, small, and highly deformable targets more precisely. By coordinating three decoding paths with different receptive fields, the model preserves complementary local-texture and global-shape cues during reconstruction, thereby sharpening boundaries and reducing interference from co-occurring background patterns.

Together, DL and the proposed task-oriented adaptive attention design form a coherent processing pipeline: DL enlarges feature dispersion, the encoder-side attention improves structure-sensitive representation learning, and the decoder-side multi-scale calibration promotes accurate recovery of fine-grained anatomical structures. This cooperative design enhances segmentation reliability across different datasets, anatomies, and imaging modalities.

Overall, the main contributions of this paper are as follows:

- We introduce a lightweight *Dispersive Loss* to alleviate feature collapse during representation learning. By enforcing all-negative constraints among in-batch embeddings, it enlarges inter-sample margins and produces more separable, boundary-aware features with near-zero inference overhead.
- We develop a task-oriented adaptive attention design for fine-grained anatomical structure segmentation. Instead of treating attention as a generic module combination, our design explicitly targets a key challenge in medical segmentation, namely the mutual interference between local texture cues and global structural shape. The encoder-side attention enhances structure-sensitive representations, while the decoder-side multi-scale calibration improves the recovery of small, deformable, and ambiguous regions.
- Extensive experiments on five datasets across three clinical modalities demonstrate the complementary benefits of dispersion regularization and adaptive fine-grained attention. Med-DisSeg achieves state-of-the-art performance with strong cross-dataset and cross-architecture generalization.

2. Related Works

2.1. Encoder–Decoder Architectures for Medical Segmentation

Encoder–decoder frameworks constitute the mainstream for medical image segmentation. U-Net (Ronneberger et al., 2015) and nnU-Net (Isensee et al., 2021) establish the dominant U-shaped paradigm, while subsequent variants incorporate boundary-aware modeling and attention modules to better preserve fine structures (Wang et al., 2022; Xu et al., 2023). Along this line, Malekmohammadi et al. enhance attentive U-Net for automated breast ultrasound mass segmentation (Malekmohammadi et al., 2024). DUNet (Jin et al., 2019) further integrates deformable convolutions to capture curvilinear structures, and MLN-net (Wang et al., 2024) introduces multi-source normalization and branch selection for cross-domain robustness. More recently, SelfReg-UNet (Zhu et al., 2024) stabilizes optimization via self-regularization, while KMUNet (Zhang et al., 2025) augments the decoder with KAN- and Mamba-based components to model long-range dependencies. Nevertheless, most of these models adopt a single-stage training pipeline and do not explicitly address representation collapse or fine-grained multi-scale calibration in a unified manner.

2.2. Attention and Transformer Mechanisms

To capture long-range dependencies and global context, attention and Transformer modules have been widely integrated into segmentation backbones. TransUNet (Chen et al., 2021) and UNETR (Hatamizadeh et al., 2022) introduce ViT-style encoders into U-shaped architectures and show clear benefits on 2D/3D medical data. TransUNet+ (Liu et al., 2022) redesigns skip connections to strengthen multi-scale feature fusion and boundary delineation. More recent designs improve efficiency or decoding, including EMCAD (Rahman et al., 2024) and HRViT (Guo et al., 2025). Related efforts such as CAFE-Net (Liu et al., 2024) and Transiam (Li et al., 2024) further exploit cross-attention and locality-aware aggregation for enhanced fusion. While these mechanisms strengthen contextual modeling, they often incur substantial complexity and may still under-emphasize boundary-sensitive details.

2.3. Representation Regularization and Contrastive Segmentation

Beyond architectural changes, representation regularization aims to increase discriminability and mitigate feature collapse. Contrast-driven frameworks learn class-separable embeddings via region-level contrast; for example, ConD-Seg (Lei et al., 2025) disentangles foreground-/background-/uncertainty and performs contrast-driven aggregation with a size-aware decoder. General contrastive objectives (SimCLR) (Chen et al., 2020) and task-specific variants such as VoCo (Wu et al., 2024) and DyCON (Assefa et al., 2025) show that dispersion-promoting learning can benefit medical segmentation, but often relies on sampling strategies or extra heads. Semi-Mamba-UNet (Ma and Wang, 2024) integrates a visual Mamba-based encoder–decoder with CNN-based

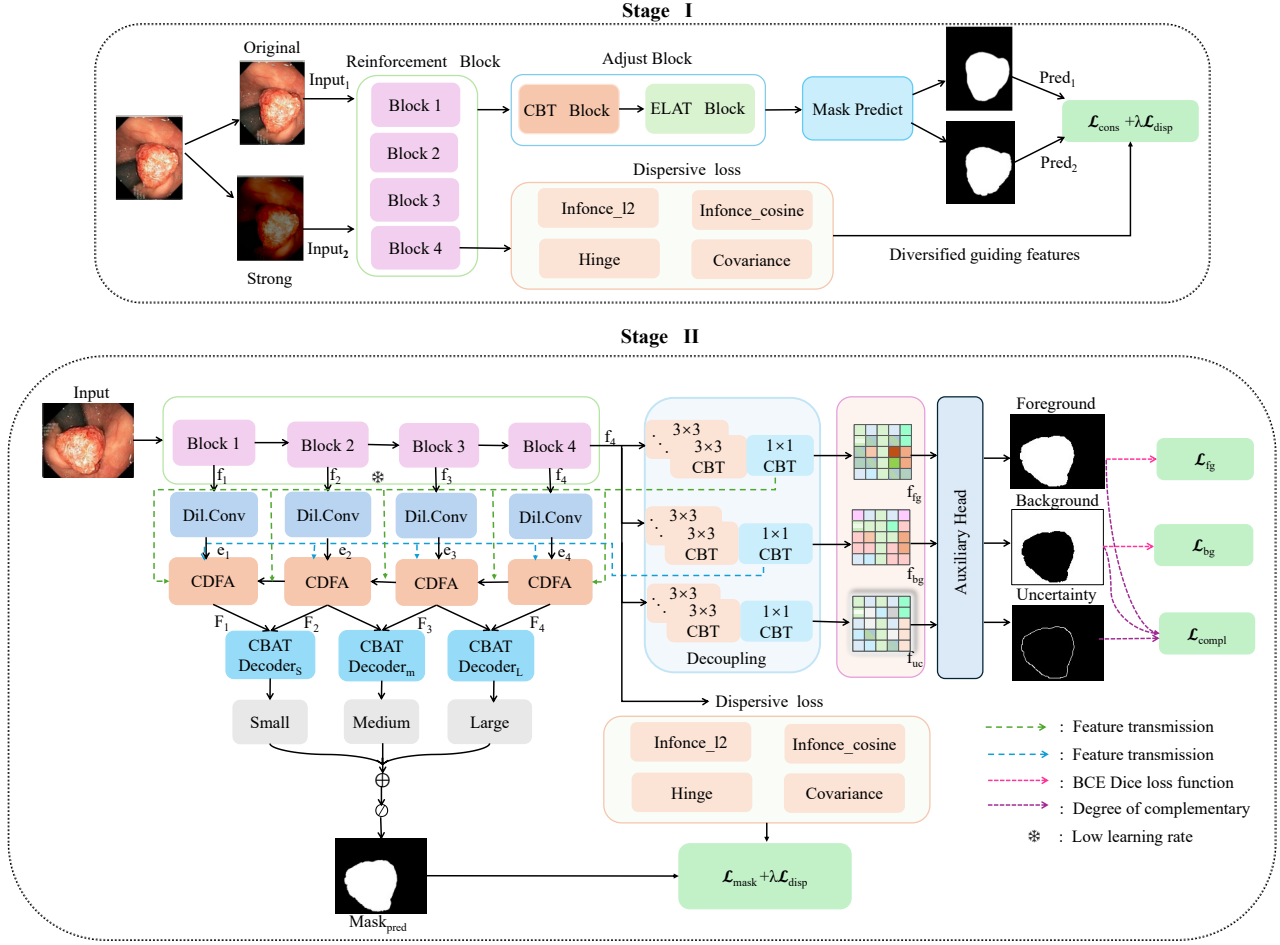


Figure 1: Overall architecture of Med-DisSeg: Stage I (top) and Stage II (bottom).

UNET and employs pixel-level contrastive learning to exploit unlabeled data, while Chen et al. combine contrastive learning with explicit shape awareness for semi-supervised segmentation (Chen et al., 2024). These observations motivate simple, sampling-free regularizers that expand inter-sample margins within mini-batches while remaining lightweight: Dispersive Loss (Wang and He, 2025) provides an elegant 'contrastive loss without positive pairs' that encourages representational diversity, yet such dispersion-based regularization has been rarely explored in medical image segmentation. Our work connects this insight with medical segmentation by integrating Dispersive Loss into a two-stage encoder–decoder framework, explicitly combating representation collapse and complementing our ELAT module and CBAT decoders to yield more separable, boundary-aware embeddings.

3. Methodology

This section first outlines the overall two-stage framework of Med-DisSeg and then presents its three cooperative components: the Dispersive Loss, the encoder-side adaptive attention mechanism, and the decoder-side multi-scale adaptive calibration strategy. Rather than functioning as isolated

modules, these components are jointly designed to address two practical challenges in medical image segmentation: avoiding representation collapse during encoding and improving fine-grained delineation of small, deformable, and low-contrast anatomical structures during decoding.

3.1. Network Architecture

Med-DisSeg follows a two-stage framework that decouples robust representation learning from multi-scale decoding (see Fig. 1). In Stage I, we focus on training a strong encoder; in Stage II, we plug this encoder into a multi-scale decoder for fine-grained segmentation.

Stage I: Robust encoder pre-training. We adopt ResNet-50 as the backbone encoder and train it in isolation under strong photometric perturbations (e.g., random brightness/contrast/saturation/hue shifts, occasional grayscale conversion, and Gaussian blur) to mimic low-illumination and low-contrast conditions. The ELAT module is attached to encoder blocks to enhance feature quality, and the encoder is optimized with a segmentation loss plus the proposed Dispersive Loss, yielding contrast-sensitive and dispersion-regularized representations. A lightweight prediction head is used only for supervision, ensuring that performance gains mainly come from the encoder and ELAT rather than extra decoding capacity.

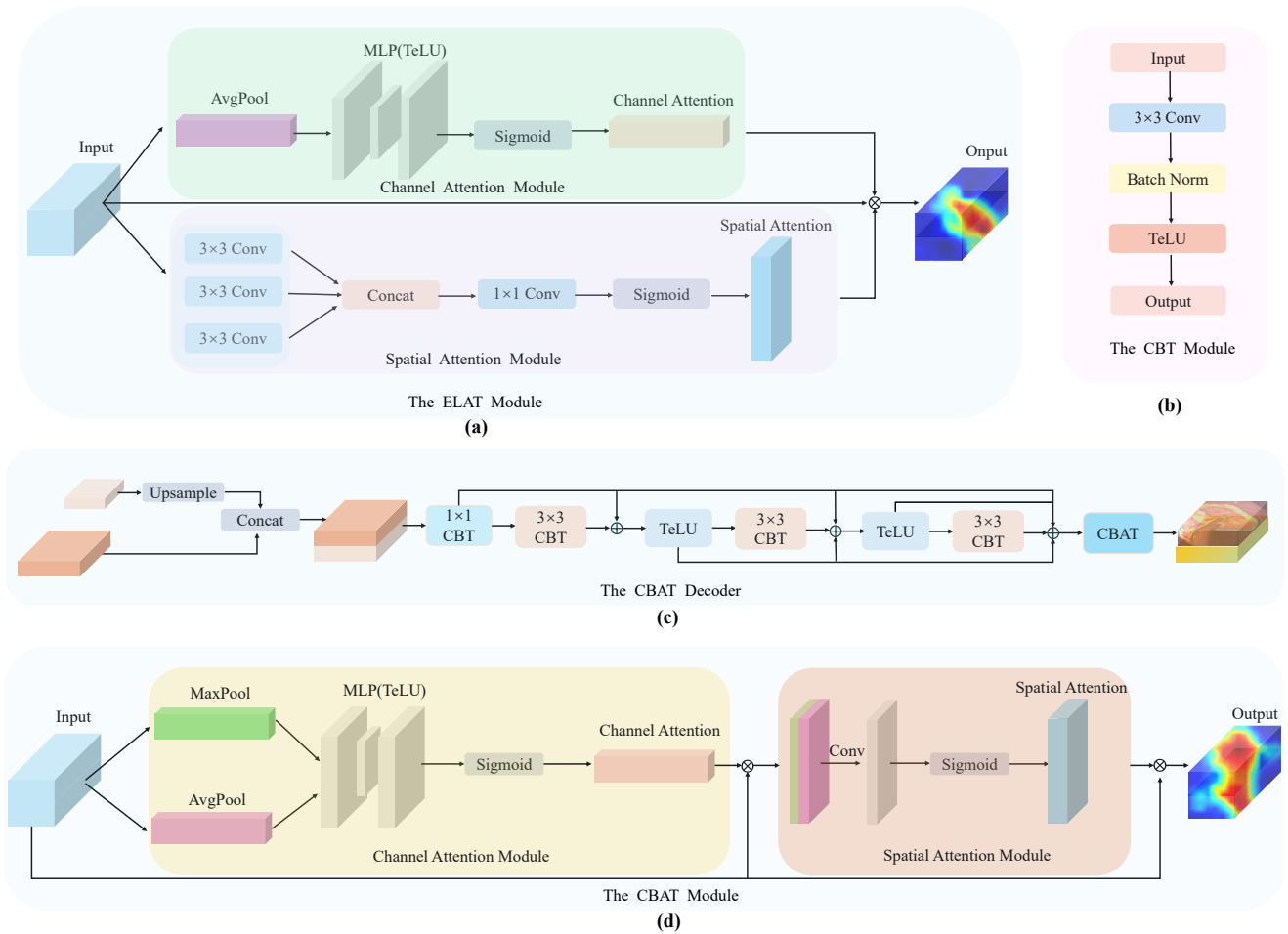


Figure 2: (a) Architecture of the ELAT module, (b) structure of the CBT blocks, (c) overall design of the CBAT-based decoder, and (d) internal structure of the CBAT module.

Stage II: Multi-scale feature decoding. In Stage II, the pre-trained encoder is integrated into the full Med-DisSeg, and the whole network is fine-tuned with a smaller learning rate, while keeping the Dispersive Loss as an auxiliary objective to maintain feature dispersion. The encoder first produces multi-level feature maps $\{f_1, \dots, f_4\}$. The deepest feature f_4 is processed by stacked CBT blocks to obtain contrast-aware foreground, background, and uncertainty maps f_{fg} , f_{bg} , and f_{uc} . These maps guide the Contrast-Driven Feature Aggregation (CDFA) module, which fuses $\{f_1, \dots, f_4\}$ across scales to enhance lesion structures and suppress distracting background patterns. Finally, three CBAT decoders D_s , D_m , and D_l operate at different resolutions to localize small, medium, and large entities, and their predictions are fused into the final segmentation mask.

This overview summarizes how Med-DisSeg couples robust representation learning with attentive multi-scale decoding to support fine-grained medical image segmentation. By strengthening feature expressiveness in the encoder and progressively aggregating hierarchical cues in the decoder, the framework better preserves small structures and delineates ambiguous boundaries. The following subsections detail the design of each component.

3.2. Overcoming feature collapse with Dispersive Loss

Medical image segmentation models are prone to feature collapse, where heterogeneous states in the hidden space are mapped to nearly identical clusters, resulting in poor feature diversity and degraded segmentation quality. To mitigate this problem in a model-agnostic manner, we introduce a **dispersive regularization** that enforces an all-negative constraint among in-batch hidden representations. By treating all pairs as negatives, this regularizer suppresses collapse and enhances inter-class separability throughout both training stages of Med-DisSeg, leading to more discriminative and stable feature embeddings.

Concretely, our Dispersive Loss encourages dispersion of hidden embeddings so that heterogeneous structures (e.g., lesion vs. normal tissue) are discouraged from collapsing into similar feature subspaces. This yields class-separable and boundary-aware representations and stabilizes optimization under heterogeneous appearances. Importantly, the Dispersive Loss is attached as an auxiliary objective in both Stage I and Stage II, acting as a global regularizer that complements architecture-level designs such as ELAT and CBAT.

The key idea of Dispersive Loss (Wang and He, 2025) is to obtain a "contrastive-style objective without explicit positive pairs". Starting from a simplified InfoNCE objective (Wang and Liu, 2021),

$$\mathcal{L}_{\text{InfoNCE}} = \frac{D(z_i, z_i^+)}{\tau} + \log \sum_j \exp\left(-\frac{D(z_i, z_j)}{\tau}\right). \quad (1)$$

where z_i and z_i^+ form a positive pair, z_j are negatives, $D(\cdot, \cdot)$ is a distance (or negative similarity), and τ is the temperature. The first term enforces positive alignment, and the second encourages dispersion among all samples. Dispersive Loss discards the alignment term and keeps only the dispersion term:

$$\mathcal{L}_{\text{Disp}} = \log \mathbb{E}_{i \neq j} \left[\exp\left(-\frac{D(z_i, z_j)}{\tau}\right) \right]. \quad (2)$$

This objective maximally spreads representations within a batch, mitigating representation collapse and improving discriminability without defining explicit positives.

In Med-DisSeg, we instantiate four variants of Dispersive Loss by removing the positive-pair alignment term from different contrastive or regularization objectives. Let $\{h_i\}_{i=1}^B$ be the batch representations, $\tau > 0$ the temperature, and $\varepsilon > 0$ a small numerical stabilizer. Self-pairs are excluded ($i \neq j$).

1. InfoNCE-based Dispersive Loss with L2 distance:

$$\mathcal{L}_{\text{disp}}^{\text{InfoNCE-L2}} = \log \left(\mathbb{E}_{i \neq j} \left[\exp(-\|h_i - h_j\|_2^2 / \tau) \right] + \varepsilon \right). \quad (3)$$

Here $D(h_i, h_j) = \|h_i - h_j\|_2^2$ measures Euclidean discrepancy in the representation space. This formulation encourages geometric separation among features, while $\varepsilon > 0$ ensures numerical stability.

2. InfoNCE-based Dispersive Loss with cosine distance:

$$\mathcal{L}_{\text{disp}}^{\text{InfoNCE-Cos}} = \log \left(\mathbb{E}_{i \neq j} \left[\exp\left(-\frac{1 - \hat{h}_i^\top \hat{h}_j}{\tau}\right) \right] + \varepsilon \right), \quad (4)$$

$$\hat{h}_i = \frac{h_i}{\|h_i\|_2}.$$

This variant relies on cosine dissimilarity $D(h_i, h_j) = 1 - \frac{h_i^\top h_j}{\|h_i\|_2 \|h_j\|_2}$, which captures angular differences between normalized representations. It is scale-invariant and focuses on directional diversity.

3. Hinge-based Dispersive Loss:

$$\mathcal{L}_{\text{disp}}^{\text{Hinge}} = \mathbb{E}_{i \neq j} \left[\max(0, \delta - \|h_i - h_j\|_2)^2 \right]. \quad (5)$$

This hinge-style formulation enforces a minimum margin δ between any pair of representations. It directly penalizes pairs that are closer than the margin, providing explicit control over the minimum dispersion distance.

4. Covariance off-diagonal penalty:

$$\mathcal{L}_{\text{disp}}^{\text{Cov}} = \sum_{p \neq q} C_{pq}^2 = \|C - \text{diag}(C)\|_F^2, \quad (6)$$

$$C = \frac{1}{B-1} \tilde{H}^\top \tilde{H}, \quad \tilde{H} = H - \mathbf{1} \bar{h}^\top.$$

where $H = [h_1^\top, \dots, h_B^\top]^\top$ and $\bar{h} = \frac{1}{B} \sum_i h_i$. This variant minimizes the off-diagonal energy of the covariance matrix computed from centered features. By discouraging cross-dimensional correlations, it promotes decorrelated and dispersed embeddings.

Overall objective. In both Stage I and Stage II, Dispersive Loss serves as a generic regularizer that pushes features away from collapse while the segmentation head and architectural modules specialize these features for mask prediction. The total loss in both stages is defined as

$$\mathcal{L}_{\text{total}} = \mathcal{L}_{\text{mask}} + \lambda \mathcal{L}_{\text{disp}}. \quad (7)$$

where $\mathcal{L}_{\text{mask}}$ denotes the segmentation loss, $\mathcal{L}_{\text{disp}}$ the chosen Dispersive Loss variant, and λ is a balancing hyperparameter. In the next subsection, we describe how ELAT and CBAT are designed to exploit these dispersion-regularized features for fine-grained and multi-scale decoding.

3.3. Enhancing fine-grained focusing and multi-scale fusion

While Dispersive Loss regularizes the geometry of feature space globally, robust medical segmentation also requires architectural guidance on *where* the network should focus and *at which scale* relevant structures should be recovered. In clinical images, accurate delineation often depends on two complementary yet potentially interfering cues: local texture variations that indicate subtle lesion boundaries, and global shape patterns that maintain anatomical plausibility. To better preserve both types of information, Med-DisSeg adopts a task-oriented adaptive attention design consisting of an encoder-side structure-sensitive attention mechanism and a decoder-side multi-scale calibration strategy. Together with Dispersive Loss, these components form an integrated framework in which dispersion regularization improves feature separability, encoder attention enhances structure-aware responses, and decoder calibration converts them into accurate segmentation masks.

3.3.1. Encoder-side adaptive attention for structure-sensitive representation learning

In two-stage segmentation frameworks, the quality of encoder representations largely determines the upper bound of downstream delineation performance. This is particularly critical in medical images, where fine-grained anatomical structures often exhibit weak contrast, ambiguous boundaries, and heterogeneous appearances. Under such conditions, local lesion texture and overall structural shape are both informative, yet they may interfere with each other if the network relies on a single undifferentiated attention pathway.

To better accommodate this characteristic, we introduce an encoder-side adaptive attention mechanism that is tailored for fine-grained anatomical structure segmentation. As shown in Fig. 2(a), this mechanism takes a feature map of size $B \times C \times H \times W$ and outputs a reweighted feature map

of the same size. It combines a channel-aware branch for capturing semantic importance and a multi-scale spatial branch for highlighting salient regions across receptive fields. Such a design enables the encoder to preserve structure-sensitive responses while remaining robust to appearance heterogeneity and low-contrast imaging conditions.

Compared with serial attention routing, this parallel formulation is better suited to retaining the relative independence of texture-oriented and shape-oriented cues during feature refinement. As a result, the encoder can produce representations that are not only more discriminative in feature space when coupled with Dispersive Loss, but also more reliable for subsequent fine-grained delineation of subtle and ambiguous structures.

3.3.2. Decoder-side multi-scale adaptive calibration for fine-grained delineation

Even with strong encoder representations, medical image decoding remains challenging because small lesions, thin structures, and highly deformable regions are easily blurred or overwhelmed during multi-scale fusion. In practice, precise reconstruction requires the decoder to preserve both fine local details and global structural coherence, rather than overemphasizing either one alone.

To address this issue, we design a decoder-side multi-scale adaptive calibration strategy with three scale-specific decoding paths, denoted by D_s , D_m , and D_l , corresponding to small (S), medium (M), and large (L) receptive fields. Instead of viewing these paths merely as parallel decoder branches, we treat them as complementary routes for recovering fine texture details, intermediate semantic organization, and global anatomical consistency, respectively. This coarse-to-fine hierarchy is naturally aligned with the multi-level features produced by the encoder and CDFA.

Specifically, D_s focuses on subtle boundaries and fine texture variations, D_m captures intermediate-scale semantic structures to preserve regional consistency, and D_l provides broader contextual support to maintain anatomical coherence. Through adaptive balancing of channel and spatial responses across the three paths, the decoder preserves the complementary roles of local-texture and global-shape information during reconstruction.

The structure of the proposed decoder is depicted in Fig. 2(c). Given two input features with different spatial resolutions, denoted by F_1 and F_2 , the decoder at level $\ell \in \{S, M, L\}$ operates as follows: (i) upsample F_1 to match the spatial size of F_2 and concatenate them; (ii) refine the concatenated feature using a stack of CBT blocks with residual shortcuts; and (iii) apply the adaptive attention unit to produce the stage output O_ℓ :

$$\begin{aligned} F_\ell^{(0)} &= [\text{Up}(F_1); F_2], \\ F_\ell^{(t+1)} &= F_\ell^{(t)} + \text{CBT}_{3 \times 3}(\text{CBT}_{1 \times 1}(F_\ell^{(t)})), \quad t = 0, 1, 2, \\ O_\ell &= \text{CBAT}(F_\ell^{(3)}). \end{aligned} \quad (8)$$

where $\ell \in \{S, M, L\}$ denotes the small-, medium-, and large-scale decoding paths, respectively. Here t indicates the iterative refinement step, $\text{Up}(\cdot)$ is the upsampling operation, $\text{CBT}(\cdot)$ the CBT block, and $\text{CBAT}(\cdot)$ the adaptive calibration unit.

The final prediction is obtained by aggregating the three scale-specific outputs as

$$O = O_S + O_M + O_L. \quad (9)$$

This aggregation fuses complementary multi-scale cues, reinforces global–local consistency, sharpens ambiguous boundaries, and improves the preservation of small anatomical structures in the final mask.

Together with Dispersive Loss and the encoder-side adaptive attention mechanism, the decoder-side multi-scale calibration strategy completes the Med-DisSeg framework by converting well-dispersed and structure-sensitive features into high-fidelity medical image segmentations.

4. Experiments

4.1. Experimental Setup

All experiments were run on a single NVIDIA GeForce RTX 4090 GPU. The input resolution was fixed to 256×256 pixels. We applied lightweight data augmentation comprising random rotations and vertical/horizontal flips. Training used mini-batches of size 4 and the Adam optimizer (Kingma and Ba, 2015). Unless otherwise stated, ResNet-50 (He et al., 2016) served as the default encoder. We adopted a two-stage schedule: in Stage I the learning rate was 1×10^{-4} for the whole network; in Stage II we initialized from the Stage I encoder and reduced the encoder’s learning rate to 1×10^{-5} while keeping 1×10^{-4} for the remaining parts. Throughout all experiments, we reproduce competing methods using their official implementations whenever available; when official code is unavailable, we report the results from the original papers and clearly indicate this in the corresponding tables/captions.

4.2. Datasets and Metrics

To assess both the effectiveness and the breadth of applicability of our approach for medical image segmentation, we evaluate it on five widely used benchmarks: Kvasir-SEG (Jha et al., 2020), Kvasir-Sessile (Jha et al., 2021), GlaS (Sirinukunwattana et al., 2017), ISIC-2016 (Gutman et al., 2016), and ISIC-2017 (Codella et al., 2019). These datasets span three medical imaging modalities and several representative segmentation subtasks, including colonoscopic polyp segmentation (Kvasir-SEG and Kvasir-Sessile), histopathology gland segmentation (GlaS), and dermoscopic skin lesion segmentation (ISIC-2016/2017). The images cover a wide range of resolutions, contrast conditions, lesion sizes and shapes, and degrees of boundary ambiguity, providing a diverse test bed for evaluating robustness and generalization.

For Kvasir-SEG, we follow the official recommendation and use an 880/120 split for training/validation. For Kvasir-Sessile—a challenging subset of Kvasir-SEG that

Table 1

Comparison with other methods on the Kvasir-Sessile, Kvasir-SEG, and GlaS datasets. **Bold** indicates best performance, underline indicates second-best.

Methods	Kvasir-Sessile				Kvasir-SEG				GlaS			
	mIoU	mDSC	Rec.	Prec.	mIoU	mDSC	Rec.	Prec.	mIoU	mDSC	Rec.	Prec.
U-Net (MICCAI 2015)	23.1	33.8	45.1	46.6	65.5	75.8	83.6	77.6	75.8	85.5	90.3	82.8
U-Net++ (MICCAI 2018)	38.4	50.2	62.5	51.8	67.9	77.2	86.5	77.7	77.6	86.9	89.6	85.5
Attn U-Net (MIDL 2018)	27.5	38.9	59.0	44.4	67.6	77.4	83.9	79.9	76.6	85.9	91.8	82.2
PraNet (MICCAI 2020)	66.7	77.4	80.7	82.4	83.0	89.4	90.6	91.3	71.8	83.0	90.9	78.0
TGANet (MICCAI 2022)	74.4	82.0	79.3	85.9	83.3	89.2	91.3	91.2	77.1	81.8	84.7	80.2
DCSAU-Net (Comput. Biol. Med. 2023)	72.6	81.1	65.6	62.9	83.5	88.9	89.5	89.5	77.6	86.5	93.0	82.5
XBFormer (TMI 2023)	73.6	81.1	87.2	76.3	83.8	89.0	89.8	87.2	73.7	84.3	84.0	85.7
CASF-Net (Comput. Biol. Med. 2023)	60.5	72.4	78.0	74.8	81.7	88.7	89.2	88.2	78.4	87.2	91.3	85.9
DTAN (KBS 2024)	76.4	84.2	84.2	85.9	84.1	90.4	<u>91.6</u>	<u>92.0</u>	78.5	87.9	88.5	90.2
DoubleAANet (Information Fusion 2025)	72.2	82.3	89.9	79.4	82.1	90.4	91.3	76.3	83.2	85.6	88.1	90.1
ConDSeg (AAAI 2025)	<u>81.2</u>	<u>89.1</u>	<u>90.1</u>	<u>90.0</u>	<u>84.6</u>	<u>90.5</u>	92.3	91.7	<u>85.1</u>	<u>91.6</u>	<u>93.5</u>	<u>90.5</u>
Ours	84.6	91.3	90.4	93.3	85.9	91.6	91.3	94.0	85.7	92.2	93.7	91.4

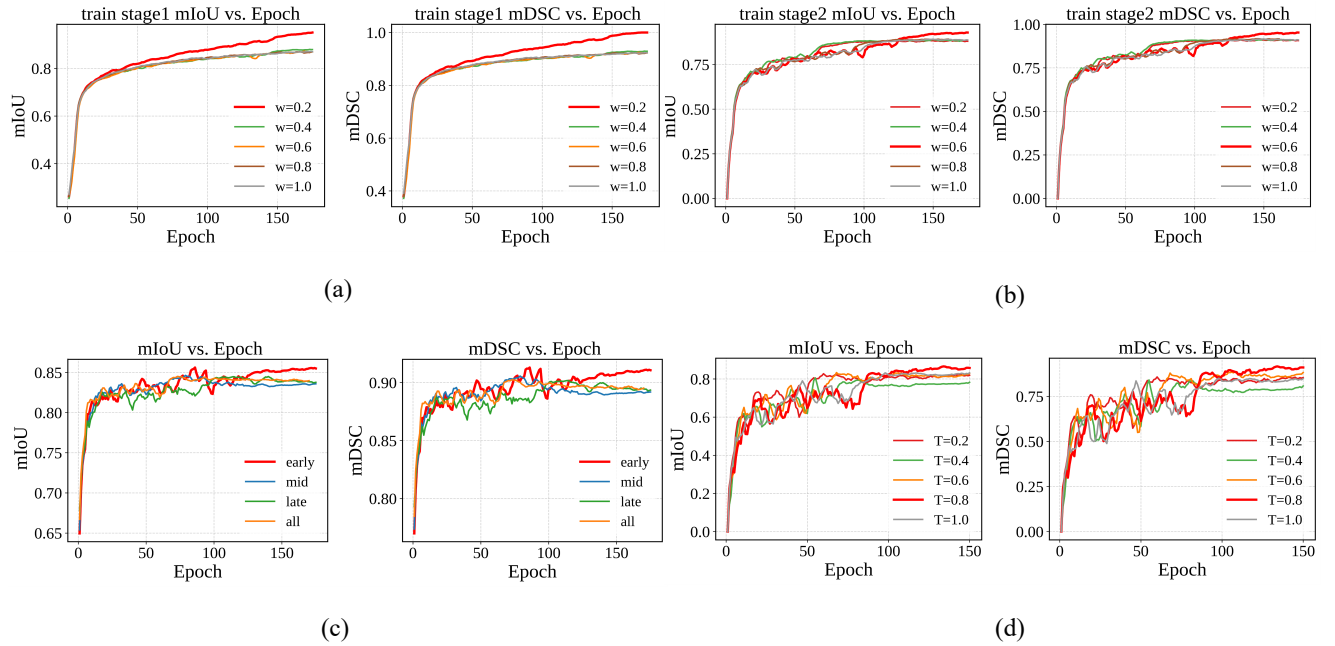


Figure 3: Hyperparameter study for the InfoNCE-L2 component of the dispersive loss. Figures (a) and (b) are about the weight, Figure (c) is about the layer placement, and Figure (d) is about the temperature.

focuses on small and flat sessile polyps—we adopt the widely used 156/20/20 split for training/validation/testing, consistent with prior work (e.g., (Tomar et al., 2022; Jha et al., 2021)). For GlaS, we use the official split of 85/80 for training/validation. For ISIC-2016, we utilize the official split of 900/379 for training/validation. For ISIC-2017, we also follow the official protocol with a 2000/150/600 split for training/validation/testing. In all experiments, the ground-truth foreground corresponds to the target anatomical structure (polyp, gland, or skin lesion), and the background contains all remaining pixels.

Performance is reported using standard medical image segmentation metrics, including mean Intersection-over-Union (mIoU), mean Dice Similarity Coefficient (mDSC),

Recall, and Precision. mIoU and mDSC both measure the overlap between the predicted mask and the ground truth and serve as our primary criteria, where mIoU reflects the average overlap ratio and mDSC can be viewed as an F1-type score. All scores are computed per image and then averaged over the test set. Recall characterizes the sensitivity to lesion pixels, while Precision measures how many predicted lesion pixels are correct, so high recall avoids missed lesions and high precision prevents over-segmentation. Unless otherwise stated, all metrics are reported in percentage form.

4.3. Comparison with Other State-of-the-Art

Tables 1 and 2 report comparisons against representative SOTA approaches, including U-Net (Ronneberger et al.,

Table 2
Comparison on ISIC-2016 and ISIC-2017 (mIoU / mDSC).

Method	ISIC-2016		ISIC-2017	
	mIoU	mDSC	mIoU	mDSC
U-Net (MICCAI 2015)	83.6	90.3	73.7	82.8
CE-Net (TMI 2019)	84.6	90.9	76.4	84.8
CPFNet (TMI 2020)	84.2	90.7	76.2	84.7
FAT-Net (Med Image Anal 2022)	85.3	91.6	76.5	85.0
DCSAU-Net Comput. Biol. Med. 2023)	85.3	91.4	76.1	85.0
EIU-Net (Comput. Biol. Med. 2023)	85.5	91.9	77.1	85.5
ADZUS (MDPI Bioengineering 2025)	86.7	92.9	80.0	88.7
CondSeg (AAAI 2025)	86.8	92.5	80.9	88.3
Ours	87.4	93.1	81.4	89.7

2015), U-Net++ (Zhou et al., 2018), Attn U-Net (Oktay et al., 2018), CE-Net (Gu et al., 2019), CPFNet (Feng et al., 2020), PraNet (Fan et al., 2020), FATNet (Wu et al., 2022), TGANet (Tomar et al., 2022), DCSAU-Net (Xu et al., 2023), XBoundFormer (Wang et al., 2023), CASF-Net (Zheng et al., 2023), EIU-Net (Yu et al., 2023), DTAN (Zhao et al., 2024), and ConDSEG (Lei et al., 2025). These baselines cover classical encoder–decoder CNNs (U-Net, U-Net++, Attn U-Net, CE-Net, CPFNet), polyp-specific and context-enhanced architectures with boundary refinement (PraNet, FATNet, TGANet, DCSAU-Net), transformer-based or hybrid models emphasizing long-range dependencies and cross-scale fusion (XBoundFormer, CASF-Net, EIU-Net, DTAN), as well as contrastive representation learning for medical segmentation (ConDSEG), thus providing a strong and diverse benchmark for evaluating Med-DisSeg.

Across all five datasets, our method achieves the best segmentation performance. Compared with the SOTA model CondSeg (Lei et al., 2025), our method achieves improvements of up to 3.4% and at least 0.5% in mIoU across the five datasets, with an average gain of approximately 1.3%. Our model delivers superior segmentation results over existing methods, particularly in preserving boundary details and detecting small structures. This can be attributed to the synergy among the proposed ELAT module, the CBAT decoder, and the Dispersive Loss. ELAT generates higher-quality encoder features, enabling the decoder to better attend to fine-grained structures and regions that are otherwise difficult to focus on. The CBAT decoder further reinforces these details through multi-scale feature fusion. Meanwhile, the Dispersive Loss effectively prevents feature collapse, enlarges inter-class margins, and guides the network toward a more discriminative feature distribution, ultimately resulting in significantly superior segmentation performance.

4.4. Ablation Study

We conducted extensive ablation studies on the proposed components, and the results are summarized as follows:

Evaluation of dispersive loss variants. To illustrate which of the four dispersive-loss variants (*InfoNCE–L2 Loss*, *InfoNCE–Cosine Loss*, *Hinge Loss*, and *Covariance Loss*) is most effective, we evaluate them on the Kvasir-SEG

dataset. For fairness, all runs adopt identical hyperparameters (loss weight = 0.5, temperature $\tau = 0.5$) and the same layer placement (*early*).

The results summarized in Fig. 4(a) show that *InfoNCE–L2 Loss* achieves the best performance, yielding the highest mIoU (85.6) and mDSC (91.2). These results represent gains of +0.5 or +0.4 over the next best *Hinge Loss*, and +0.9 or +0.6 over *InfoNCE–Cosine Loss*.

We analyze that the squared ℓ_2 distance induces stronger geometric separation in the embedding space, while cosine dissimilarity—being scale-invariant—may underutilize magnitude cues that are critical for boundary-sensitive segmentation. The *Covariance Loss* reduces feature redundancy but yields smaller overall improvements.

Overall, these results indicate that InfoNCE-style dispersion with ℓ_2 distance provides the most effective regularization under our settings.

Dispersive Loss hyperparameter study. To verify the influence of each parameter, we further investigate the sensitivity of the Dispersive Loss to its key design choices on Kvasir-SEG. Specifically, we sweep the temperature $\tau \in \{0.2, 0.4, 0.6, 0.8, 1.0\}$, the loss weight $\lambda \in \{0.2, 0.4, 0.6, 0.8, 1.0\}$, and the layer placement (*early* in the encoder, *middle* around the bottleneck, and *late* in the decoder).

The curves in Fig. 3 reveal several consistent trends aligned with our two-stage training strategy. First, for the Stage I loss weight sweep (Fig. 3(a)), the optimum occurs at $\lambda_1 = 0.2$. Very small weights under-regularize ($\lambda_1 < 0.2$), failing to shape the representation space, whereas larger values ($\lambda_1 > 0.2$) over-constrain early optimization. This suggests that insufficient regularization fails to prevent feature collapse and promote representation diversity, while excessive values interfere with task-relevant learning, highlighting the need for balanced dispersive regularization.

Second, for the Stage II sweep (Fig. 3(b)), the best setting is $\lambda_2 = 0.6$. Since the Stage II encoder fine-tunes the pre-trained encoder from Stage I, a larger weight is required to impose stronger dispersion and refine inter-class boundary features.

Third, for layer placement (Fig. 3(c)), applying the Dispersive Loss *early* in the encoder outperforms *middle*, *late*, and *all*. This indicates that injecting dispersion at early layers more effectively structures the embedding space and benefits downstream decoding.

Fourth, regarding the temperature parameter (Fig. 3(d)), performance peaks at $\tau = 0.8$. Too small τ produces overly sharp penalties that destabilize optimization, whereas too large τ weakens the contrast signal.

Unless otherwise specified, we adopt $(\lambda_1, \lambda_2) = (0.2, 0.6)$, *early* placement, and $\tau = 0.8$ in subsequent experiments.

Contribution analysis of the proposed design. To quantify the contribution of each part of the framework, we conduct an ablation study on the Kvasir-SEG dataset, as summarized in Table 3. Starting from a baseline without our proposed designs, introducing the encoder-side adaptive attention and the decoder-side multi-scale calibration each

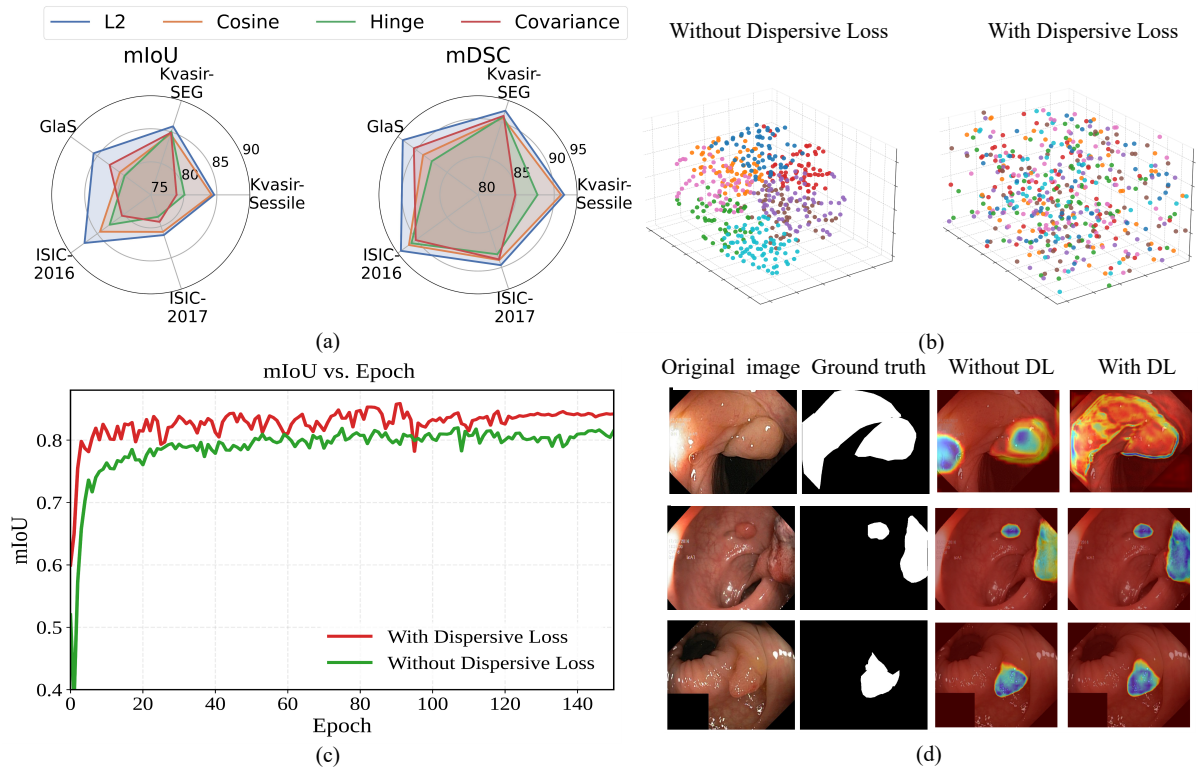


Figure 4: (a) Four types of Dispersion Loss in the effect graphs of five datasets. (b) Feature distributions with and without Dispersive Loss, showing broader inter-sample dispersion when it is applied. (c) mIoU comparison with and without Dispersive Loss. (d) Grad-CAM maps with and without Dispersive Loss.

Table 3
Evaluation on Kvasir-SEG dataset of the ELAT module, CBAT decoder, and Dispersive Loss applied in two stages.

Variant	Backbone	ELAT	CBAT	Disp-I	Disp-II	mIoU	mDSC
1	✓	✗	✗	✗	✗	84.3	89.7
2	✓	✓	✗	✗	✗	85.0	90.8
3	✓	✗	✓	✗	✗	84.6	90.2
4	✓	✓	✓	✗	✗	85.2	91.1
5	✓	✓	✓	✓	✗	85.4	91.3
6	✓	✓	✓	✗	✓	85.6	91.4
7	✓	✓	✓	✓	✓	85.9	91.6

leads to clear improvements in both mIoU and mDSC. When the two are combined, the gains become larger, indicating that structure-sensitive representation enhancement in the encoder and fine-grained multi-scale recovery in the decoder play complementary roles.

Applying the Dispersive Loss in either Stage I or Stage II further improves performance, confirming the benefit of dispersion-based regularization during training. When used in both stages, the performance gains are the most pronounced, suggesting that maintaining feature dispersion throughout the two-stage optimization process helps alleviate representation collapse and improves discriminability for downstream segmentation.

Overall, the full configuration achieves the best performance across all evaluation metrics. These results verify not only the effectiveness of each component, but also the synergy among dispersion regularization, encoder-side structure-aware enhancement, and decoder-side fine-grained multi-scale reconstruction.

Comparison of decoder-side attention designs under the same baseline. To examine the compatibility between different lightweight attention designs and the decoder, we compare several representative attention mechanisms, including SE (Hu et al., 2018), ES-UNet (Park et al., 2025), CBAM (Woo et al., 2018), EMCAD (Rahman et al., 2024), LEGO-Net (Xu et al., 2025), and DA-TransUNet (Sun et al., 2024), with our decoder-side adaptive calibration design implemented by CBAT on the Kvasir-SEG dataset.

To ensure a fair comparison, we keep the backbone, decoder, and training pipeline identical and only replace the attention unit at the same decoder location. All runs use the same input resolution (256×256), data splits, augmentations, optimizer (Adam), learning-rate schedule (cosine; base LR 1×10^{-4}), weight decay, batch size (4), number of epochs (300), and early-stopping patience (100). We also adopt the same initialization (ImageNet-pretrained ResNet-50 encoder) and disable any attention-specific add-ons, such as extra normalization or additional heads. Therefore, performance differences can be attributed to the decoder-side

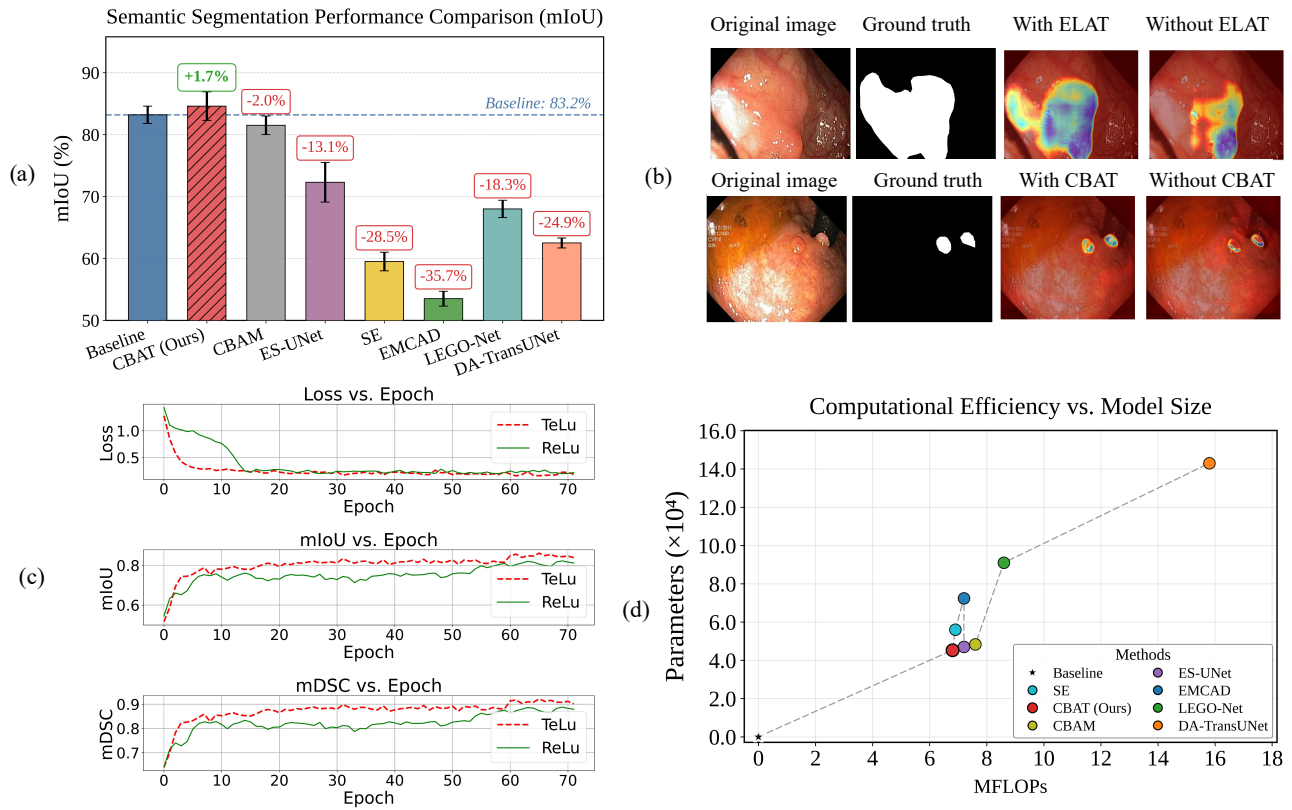


Figure 5: (a) represents the performance comparison of various attention mechanisms. (b) Comparison of attention between the presence and absence of ELAT and CBAT modules. (c) Comparison of the two activation functions: TeLU and ReLU. (d) shows the comparison of parameters and computational costs.

Table 4

Organ-wise performance of different methods on the Synapse dataset reported as DSC (%).

Organ	UNet (MICCAI 2015)	TransUNet (MICCAI 2022)	TransNorm (IEEE Access 2022)	MT-UNet (IEEE ICIP 2020)	SwinUNet (ECCV 2022)	ConDSeg (AAAI 2025)	WMREN (IJCAI 2025)	Ours
Aorta	89.1	87.2	86.2	87.9	85.5	86.6	88.9	87.6
Gallbladder	69.7	63.1	65.1	65.0	66.5	72.5	74.6	76.2
Left kidney	77.8	81.9	82.2	81.5	83.3	85.1	88.5	81.6
Right kidney	68.6	77.0	78.6	77.3	79.6	78.6	84.2	84.0
Liver	93.4	94.1	94.2	93.1	94.3	90.5	95.1	94.3
Pancreas	54.0	55.9	55.3	59.5	56.6	61.2	69.6	72.4
Spleen	86.7	85.1	89.5	87.8	90.7	87.3	91.1	91.0
Stomach	75.6	75.6	76.0	76.8	76.6	79.8	83.1	80.1
Mean DSC (%) \uparrow	76.9	77.5	78.4	78.6	79.1	80.2	84.4	83.4

attention design itself rather than other architectural or optimization factors.

To further isolate the practical overhead of the compared designs, all variants are inserted at the exact same decoder position under identical training and inference settings, and the reported results are averaged over three random seeds. The experimental results are shown in Fig. 5(a).

As shown in the figure, our decoder-side adaptive calibration design achieves the highest mean mIoU, with a relative improvement of 1.7% over the baseline. In contrast, the other compared attention mechanisms do not yield comparable gains when directly plugged into the same decoder

position. We believe this is because our design is more compatible with the requirements of fine-grained medical image decoding: it preserves the complementary roles of channel-wise semantic emphasis and spatially localized responses, while remaining lightweight enough to avoid disrupting multi-scale feature fusion.

Moreover, as illustrated in Fig. 5(b), the proposed design also shows favorable efficiency, providing the best trade-off between segmentation accuracy, parameter count, and computational cost among the compared attention mechanisms.

Activation-function validation. In the encoder-side adaptive attention and the decoder-side calibration design, we replace ReLU with the TeLU activation function. To

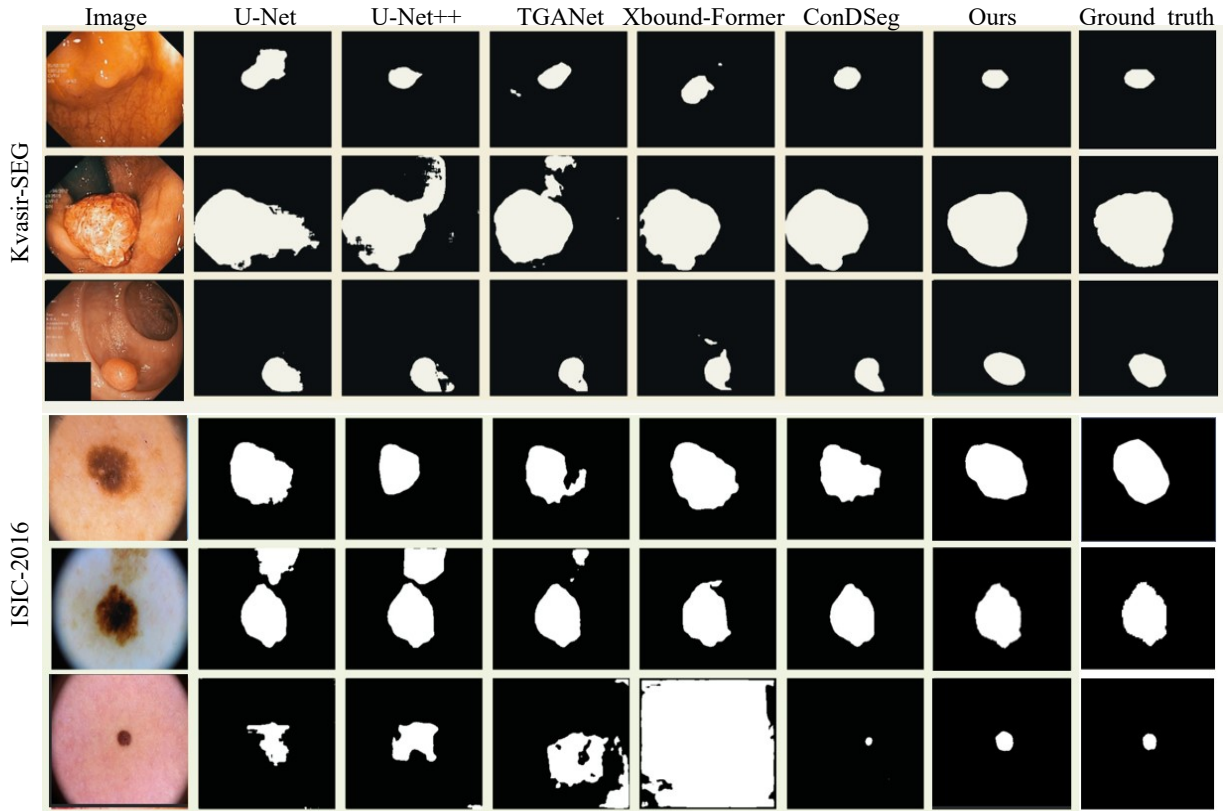


Figure 6: Visualisation of segmentation results of different models on the Kvasir-SEG and ISIC-2016 datasets.

evaluate its effect, we compare TeLU ($\phi_{\text{TeLU}}(t) = t \tanh(\exp t)$) and the standard ReLU under identical training settings.

As shown in Fig. 5(c), TeLU exhibits faster optimization in the early training stage, with a steeper drop in training loss. It also yields consistently higher validation curves for both mIoU and mDSC throughout the training process. In addition, the optimization trajectories are smoother and less oscillatory, suggesting improved training stability.

A possible explanation is that TeLU provides a smoother transition around zero and maintains nonvanishing gradients on the negative side, which helps preserve stable gradient propagation across the encoder–decoder network; further details are provided in Appendix A.1. Importantly, this substitution introduces negligible computational overhead relative to ReLU. Overall, these results indicate that TeLU is a more suitable activation choice than ReLU in our framework, as it facilitates convergence and improves segmentation quality.

4.5. Generalization Experiment

To further evaluate the generalizability of our framework, we extend Med-DisSeg to a multi-class 3D abdominal organ segmentation setting on the Synapse dataset. Following the protocols of TransUNet and SwinUNet, each 3D CT volume is decomposed into a sequence of 2D slices and trained in a slice-wise manner. To accommodate the multi-organ setting, the original binary cross-entropy loss is replaced with a multi-class cross-entropy loss for segmenting

eight abdominal organs. Compared with the binary lesion-oriented datasets used in the main experiments, Synapse presents a more challenging testbed due to its larger anatomical diversity, covering both large and compact organs (e.g., liver and spleen) and small, thin, or highly shape-variant structures (e.g., pancreas and gallbladder). The organ-wise Dice scores are reported in Table 4.

Overall, Med-DisSeg achieves a mean DSC of 83.4%, outperforming all CNN- and Transformer-based competitors such as UNet (76.9%), TransUNet (77.5%), MT-UNet (78.6%), SwinUNet (79.1%), and ConDSeg (80.2%), and ranking second among all compared methods. These results indicate that the proposed framework transfers effectively from 2D binary medical segmentation tasks to a more complex multi-class abdominal CT scenario.

A closer examination of the organ-wise results reveals that Med-DisSeg maintains strong and stable performance across most organs. In particular, it achieves the best Dice scores on the gallbladder (76.2%) and pancreas (72.4%), while also obtaining competitive results on the right kidney (84.0%), liver (94.3%), spleen (91.0%), and stomach (80.1%). This trend suggests that the proposed framework is especially effective for anatomically challenging targets with small size, weak boundaries, or large shape variations.

When grouping organs by size and structural complexity, the improvement pattern becomes clearer. For large and relatively regular organs such as the liver and spleen, performance gains are relatively limited, largely because

existing methods already achieve high Dice scores on these easier structures. In contrast, the benefits are more pronounced on small, thin, and deformable organs such as the pancreas and gallbladder. This observation is consistent with the design motivation of Med-DisSeg: dispersion regularization helps maintain feature separability, while the encoder-side structure-sensitive enhancement and decoder-side fine-grained multi-scale reconstruction are better suited to preserving subtle boundaries and recovering anatomically ambiguous structures.

Compared with the current SOTA WMREN model (Lu et al., 2025), which is specifically tailored for Synapse, Med-DisSeg achieves a comparable mean DSC (83.4% vs. 84.4%) and remains highly competitive across most organs. Notably, Med-DisSeg surpasses WMREN on difficult small organs such as the gallbladder (76.2% vs. 74.6%) and pancreas (72.4% vs. 69.6%), while achieving similar performance on large organs such as the liver and spleen. These results demonstrate that Med-DisSeg not only generalizes well to a new imaging modality (CT), but also adapts robustly to diverse anatomical scales and geometries, particularly in settings that require fine-grained delineation of small and structurally complex organs.

4.6. Visualization Analysis

Fig. 6 presents qualitative comparisons on the Kvasir-SEG and ISIC-2016 datasets. Compared with typical encoder-decoder baselines and recent state-of-the-art methods, Med-DisSeg produces segmentation masks with sharper boundaries, more complete recovery of small or low-contrast lesions, and fewer false responses in surrounding background regions. These visual improvements are consistent with the quantitative gains reported in Tables 1 and 2.

Fig. 4(b) provides a feature-space view of the effect of dispersion regularization. Without the Dispersive Loss, foreground and background representations tend to collapse into a few dense clusters, reducing inter-class separability and making downstream segmentation more ambiguous. By contrast, when dispersion regularization is applied, the feature distribution becomes more separated and structured, which is more favorable for boundary-aware prediction.

Fig. 4(c) further supports this observation through the training curves. With the Dispersive Loss enabled, the model achieves consistently higher mIoU throughout training, together with faster convergence and a smoother optimization trajectory. In contrast, the model trained without dispersion regularization shows more noticeable fluctuations and earlier performance saturation, which is consistent with the collapsed feature patterns observed in Fig. 4(b).

Fig. 4(d) visualizes the corresponding response maps. Without dispersion regularization, activations tend to leak into irrelevant background areas and become fragmented around ambiguous boundaries, especially under co-occurring textures or low-contrast conditions. With the Dispersive Loss, the responses become sharper and more spatially coherent, better aligned with the target semantic regions, and less affected by distracting structures. These observations

suggest that improving feature separability in the embedding space also benefits downstream localization and boundary discrimination.

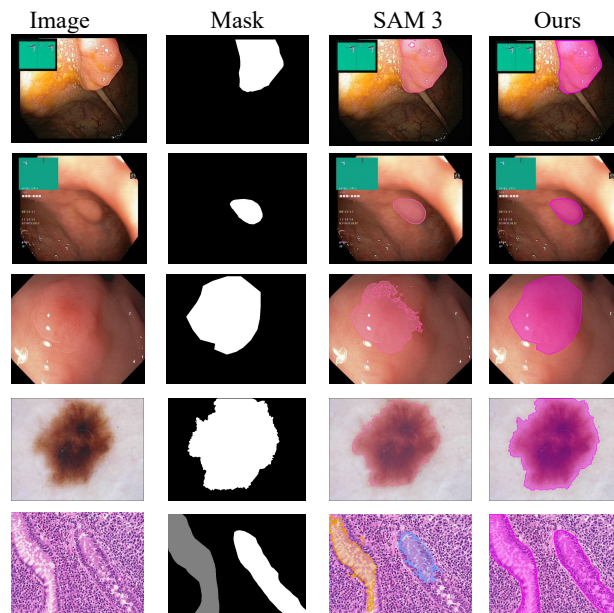


Figure 7: Visual comparison with the SAM 3 model.

Fig. 5(d) illustrates the effect of the proposed fine-grained attention design on intermediate responses. When the encoder-side structure-sensitive enhancement is removed, activations become more diffuse and are more easily distracted by specular highlights or background textures. In contrast, with the encoder-side attention enabled, the network responds more consistently to true lesion regions, particularly around weak or fuzzy boundaries. On the decoder side, the multi-scale reconstruction paths exhibit complementary behaviors: the small-scale path emphasizes fine details and tiny structures, while the large-scale path helps preserve global shape consistency. Their combination leads to more stable and coherent multi-scale recovery.

Beyond conventional encoder-decoder baselines, we further compare Med-DisSeg with the open-vocabulary segmentation model SAM 3 (Kirillov et al., 2025), as shown in Fig. 7. Although SAM 3 demonstrates strong generalization on natural images, its predictions on medical images remain less reliable: it tends to under-segment flat sessile polyps, produce fragmented masks around fuzzy boundaries, and respond sensitively to low-contrast textures and specular highlights. In contrast, Med-DisSeg yields more complete lesion coverage and smoother, anatomically plausible contours across diverse modalities, including endoscopy, dermoscopy, and histopathology. This difference is consistent with the design motivation of our framework, which explicitly strengthens feature separability, structure-sensitive encoding, and fine-grained multi-scale reconstruction for medical image segmentation, whereas prompt-driven foundation models such as SAM 3 are not specifically optimized for these domain-specific challenges.

Table 5

Number of learnable parameters for different models at an input size of 256×256 .

Method	#Params (M)
TGANet	19.84
XBound-Former	17.24
ConDSeg	45.55
Ours (Med-DisSeg)	45.56

Table 6

Inference speed on an NVIDIA GeForce RTX 4090 (fps).

Method	TGANet	XBound-Former	ConDSeg	Ours
FPS	32.7	61.3	59.6	59.6

Overall, the visual results consistently indicate that dispersion regularization, encoder-side structure-sensitive enhancement, and decoder-side fine-grained multi-scale reconstruction complement each other in improving boundary localization, preserving subtle structures, and suppressing background interference in challenging medical image segmentation scenarios.

4.7. Computational Analysis

To assess the computational footprint of Med-DisSeg, we compare the number of learnable parameters with several representative baselines at an input size of 256×256 . As summarized in Table 5, TGANet and XBound-Former are relatively lightweight with 19.84M and 17.24M parameters, respectively, whereas ConDSeg and our Med-DisSeg operate in a higher-capacity regime (45.55M vs. 45.56M). Importantly, Med-DisSeg maintains almost the same parameter count as ConDSeg, yet consistently achieves higher mIoU/mDSC across five benchmarks, indicating that the performance gains primarily stem from our dispersive regularization and ELAT/CBAT design rather than increased model capacity.

All inference speed (FPS) results reported in Table 6 were measured on a single NVIDIA RTX 4090 with an input size of 256×256 and a fixed batch size of 4. We report the average throughput over multiple runs after a short warm-up stage, and the timing excludes data loading and disk I/O, focusing on the pure model forward pass. Our model achieved an inference speed of 59.6 fps, fully meeting the needs for real-time segmentation.

5. Conclusion

This work addresses two practical challenges in medical image segmentation, namely representation collapse during encoding and insufficient fine-grained delineation during decoding, by proposing Med-DisSeg, a concise and effective framework that combines dispersion regularization with task-oriented adaptive attention. The proposed Dispersive Loss enlarges inter-sample margins within each batch, alleviating feature collapse and improving feature separability

without increasing inference overhead. Building on these dispersion-regularized representations, Med-DisSeg further strengthens structure-sensitive encoding and fine-grained multi-scale reconstruction, thereby improving boundary localization and the recovery of small, deformable, and low-contrast targets.

Extensive experiments on five datasets across three clinical scenarios demonstrate that Med-DisSeg consistently achieves state-of-the-art performance in terms of both mIoU and mDSC. Additional ablation, visualization, and generalization studies further verify that dispersion regularization, encoder-side structure-sensitive enhancement, and decoder-side multi-scale reconstruction contribute complementary benefits within a unified framework. These results indicate that Med-DisSeg provides an effective and generalizable solution for robust medical image segmentation, especially in challenging scenarios involving ambiguous boundaries, heterogeneous appearances, and fine-grained anatomical structures.

References

- Assefa, M., et al., 2025. Dycon: Dynamic uncertainty-aware consistency and contrastive learning for semi-supervised medical image segmentation, in: Proceedings of the IEEE/CVF Conference on Computer Vision and Pattern Recognition (CVPR), pp. 30850–30860.
- Chen, J., Lu, Y., Yu, Q., Luo, X., Adeli, E., Wang, Y., Lu, L., Yuille, A.L., Zhou, Y., 2021. Transunet: Transformers make strong encoders for medical image segmentation. arXiv preprint arXiv:2102.04306 .
- Chen, T., Kornblith, S., Norouzi, M., Hinton, G., 2020. A simple framework for contrastive learning of visual representations, in: Proceedings of the International Conference on Machine Learning (ICML), PMLR. pp. 1597–1607.
- Chen, Y., Chen, F., Huang, C., 2024. Combining contrastive learning and shape awareness for semi-supervised medical image segmentation. Expert Systems with Applications 242, 122567. doi:10.1016/j.eswa.2023.122567.
- Codella, N., et al., 2019. Skin lesion analysis toward melanoma detection 2018: A challenge hosted by the international skin imaging collaboration (isic). arXiv preprint arXiv:1902.03368 .
- Fan, D.P., et al., 2020. Pranut: Parallel reverse attention network for polyp segmentation, in: MICCAI, pp. 263–273.
- Feng, S., et al., 2020. Cpfnet: Context pyramid and feature fusion network for medical image segmentation. Neurocomputing 376, 222–235.
- Gu, Z., et al., 2019. Ce-net: Context encoder network for 2d medical image segmentation. IEEE Transactions on Medical Imaging 38, 2281–2292.
- Guo, Y., et al., 2025. Hrvit: Edge-aware token halting for efficient and accurate 3d medical image segmentation, in: Medical Image Computing and Computer-Assisted Intervention (MICCAI), pp. 1–10.
- Gutman, D., et al., 2016. Skin lesion analysis toward melanoma detection: A challenge at the isic 2016, in: IEEE International Symposium on Biomedical Imaging (ISBI) Challenge, pp. 1–10.
- Hatamizadeh, A., Tang, Y., Nath, V., Yang, D., Myronenko, A., Landman, B., Roth, H.R., Xu, D., 2022. Unetr: Transformers for 3d medical image segmentation, in: Proceedings of the IEEE/CVF Winter Conference on Applications of Computer Vision (WACV), pp. 574–584.
- He, K., Zhang, X., Ren, S., Sun, J., 2016. Deep residual learning for image recognition, in: Proceedings of the IEEE/CVF Conference on Computer Vision and Pattern Recognition (CVPR), pp. 770–778.
- Hu, J., Shen, L., Sun, G., 2018. Squeeze-and-excitation networks, in: Proceedings of the IEEE Conference on Computer Vision and Pattern Recognition (CVPR), pp. 7132–7141.
- Isensee, F., Jaeger, P.F., Kohl, S.A.A., Petersen, J., Maier-Hein, K.H., 2021. nnu-net: A self-configuring method for deep learning-based biomedical image segmentation. Nature Methods 18, 203–211.

- Jha, D., Smedsrud, P.H., Riegler, M.A., Halvorsen, P., de Lange, T., Johansen, D., Johansen, H.D., 2020. Kvasir-seg: A segmented polyp dataset, in: International Conference on Multimedia Modeling (MMM), pp. 451–462.
- Jha, D., et al., 2021. Kvasir-sessile: A polyp segmentation dataset with sessile and pedunculated annotations. *Data in Brief*.
- Jin, Q., Meng, Z., Pham, T.D., Chen, Q., Wei, L., Su, R., 2019. Dunet: A deformable network for retinal vessel segmentation. *Knowledge-Based Systems* 178, 149–162. URL: <https://www.sciencedirect.com/science/article/pii/S0950705119301984>, doi:10.1016/j.knsys.2019.04.025.
- Kingma, D.P., Ba, J., 2015. Adam: A method for stochastic optimization. *International Conference on Learning Representations (ICLR)*.
- Kirillov, A., Mintun, E., Ravi, N., Mao, H., Tejjani, R., Darrell, T., Dollár, P., Girshick, R., 2025. Segment anything model 3. *arXiv preprint arXiv:2511.16719* URL: <https://arxiv.org/abs/2511.16719>.
- Lei, M., Wu, H., Lv, X., Wang, X., 2025. Condseg: A general medical image segmentation framework via contrast-driven feature enhancement, in: *Proceedings of the AAAI Conference on Artificial Intelligence, Chicago*. pp. 4571–4579.
- Li, X., Ma, S., Xu, J., Tang, J., He, S., Guo, F., 2024. Transiam: Aggregating multi-modal visual features with locality for medical image segmentation. *Expert Systems with Applications* 237, 121574. doi:10.1016/j.eswa.2023.121574.
- Liu, G., Yao, S., Liu, D., Chang, B., Chen, Z., Wang, J., Wei, J., 2024. Cafe-net: Cross-attention and feature exploration network for polyp segmentation. *Expert Systems with Applications* 238, 121754. doi:10.1016/j.eswa.2023.121754.
- Liu, Y., Wang, H., Chen, Z., Huangliang, K., Zhang, H., 2022. Transunet+: Redesigning the skip connection to enhance features in medical image segmentation. *Knowledge-Based Systems* 256, 109859. URL: <https://www.sciencedirect.com/science/article/pii/S0950705122009522>, doi:10.1016/j.knsys.2022.109859.
- Lu, H., et al., 2025. Wavelet multi-scale region-enhanced network for medical image segmentation, in: *Proceedings of IJCAI 2025*, pp. 1–10.
- Ma, C., Wang, Z., 2024. Semi-mamba-unet: Pixel-level contrastive and cross-supervised visual mamba-based unet for semi-supervised medical image segmentation. *Knowledge-Based Systems* 300, 112203. URL: <https://www.sciencedirect.com/science/article/pii/S0950705124008372>, doi:10.1016/j.knsys.2024.112203.
- Malekmohammadi, A., Soryani, M., Kozegar, E., 2024. Mass segmentation in automated breast ultrasound using an enhanced attentive unet. *Expert Systems with Applications* 245, 123095. doi:10.1016/j.eswa.2023.123095.
- Oktay, O., Schlemper, J., Le Folgoc, L., Lee, M., Heinrich, M., Misawa, K., Mori, K., McDonagh, S., Hammerla, N., Kainz, B., et al., 2018. Attention u-net: Learning where to look for the pancreas. *arXiv preprint arXiv:1804.03999*.
- Park, M., et al., 2025. Es-unet: Efficient 3d medical image segmentation with enhanced skip connections in 3d u-net. *BMC Medical Imaging* 25, 365.
- Rahman, M.M., Munir, M., Marculescu, R., 2024. Emcad: Efficient multi-scale convolutional attention decoding for medical image segmentation, in: *Proceedings of the IEEE/CVF Conference on Computer Vision and Pattern Recognition (CVPR)*, pp. 1–10.
- Ronneberger, O., Fischer, P., Brox, T., 2015. U-net: Convolutional networks for biomedical image segmentation, in: *International Conference on Medical Image Computing and Computer-Assisted Intervention (MICCAI)*, Springer. pp. 234–241.
- Sirinukunwattana, K., et al., 2017. Gland segmentation in colon histology images: The glas challenge contest and dataset. *Scientific Reports* 7, 12821.
- Sun, G., et al., 2024. Da-transunet: Integrating spatial and channel dual attention with transformer-based u-net for enhanced medical image segmentation. *Frontiers in Bioengineering and Biotechnology* 12, 1398237.
- Tomar, N., Jha, D., Bagci, U., Ali, S., 2022. Tganet: Text-guided attention for improved polyp segmentation, in: *Medical Image Computing and Computer-Assisted Intervention (MICCAI)*, Springer. pp. 151–160.
- Wang, F., Liu, H., 2021. Understanding the behavior of contrastive loss, in: *Proceedings of the IEEE/CVF Conference on Computer Vision and Pattern Recognition (CVPR)*, pp. 2495–2504.
- Wang, J., et al., 2023. Xboundformer: Toward cross-scale boundary modeling in transformers. *IEEE Transactions on Medical Imaging* 42, 1735–1745.
- Wang, K., Ye, Z., Xie, X., Cui, H., Chen, T., Liu, B., 2024. Mln-net: A multi-source medical image segmentation method for clustered microcalcifications using multiple layer normalization. *Knowledge-Based Systems* 283, 111127. URL: <https://www.sciencedirect.com/science/article/pii/S0950705123008778>, doi:10.1016/j.knsys.2023.111127.
- Wang, R., He, K., 2025. Diffuse and disperse: Image generation with representation regularization. *arXiv preprint arXiv:2506.09027*.
- Wang, R., et al., 2022. Boundary-aware context neural network for medical image segmentation. *Medical Image Analysis* 78, 102395.
- Woo, S., Park, J., Lee, J.Y., Kweon, I.S., 2018. Cbam: Convolutional block attention module, in: *Proceedings of the European Conference on Computer Vision (ECCV)*, pp. 3–19.
- Wu, L., Zhuang, J., Chen, H., 2024. Voco: A simple-yet-effective volume contrastive learning framework for 3d medical image analysis, in: *Proceedings of the IEEE/CVF Conference on Computer Vision and Pattern Recognition (CVPR)*, pp. 1–10.
- Wu, X., Li, Z., et al., 2022. Fat-net: Feature-adaptive transformers for polyp segmentation. *Computers in Biology and Medicine* 146, 105676.
- Xu, L., et al., 2025. Lego-net: Medical image segmentation model based on local enhancement driven global optimization. *Scientific Reports* 15, 2393.
- Xu, Z., Zhang, W., et al., 2023. Dcsau-net: Dual-channel and spatial attention u-net for medical image segmentation. *IEEE Access* 11, 1–12.
- Yu, Z., et al., 2023. Eiu-net: Enhanced feature extraction and improved skip connections in u-net for skin lesion segmentation. *Computers in Biology and Medicine* 162, 107081.
- Zhang, H., et al., 2025. Kmunet: A novel medical image segmentation model based on kan and mamba, in: *Medical Image Computing and Computer-Assisted Intervention (MICCAI)*, pp. 1–10.
- Zhao, Y., et al., 2024. Dtan: Diffusion-based text attention network for medical image segmentation. *Computers in Biology and Medicine* 168, 107728.
- Zheng, J., et al., 2023. Casf-net: Cross-attention and cross-scale fusion network for medical image segmentation. *Computer Methods and Programs in Biomedicine* 229, 107307.
- Zhou, Z., Siddiquee, M.M.R., Tajbakhsh, N., Liang, J., 2018. Unet++: A nested u-net architecture for medical image segmentation, in: *International Workshop on Deep Learning in Medical Image Analysis*, Springer. pp. 3–11.
- Zhu, W., et al., 2024. Selfreg-unet: Self-regularized unet for medical image segmentation, in: *Medical Image Computing and Computer-Assisted Intervention (MICCAI)*, Springer. pp. 1–10.

A. Appendix

A.1. TeLU: Properties and Proof Sketches

We adopt TeLU

$$\phi(t) = t \tanh(e^t), \quad t \in \mathbb{R}. \quad (10)$$

Notation. Let $u = e^t (> 0)$ and write $\operatorname{sech}(x) = 1/\cosh(x)$. Then

$$\begin{aligned} \phi'(t) &= \tanh(u) + t u \operatorname{sech}^2(u), \\ \phi''(t) &= u \operatorname{sech}^2(u) + (1+t)u \operatorname{sech}^2(u) \\ &\quad - 2t u^2 \tanh(u) \operatorname{sech}^2(u). \end{aligned} \quad (11)$$

Lemma A.1 (Smoothness, growth and asymptotics). $\phi \in C^\infty(\mathbb{R})$, $|\phi(t)| \leq |t|$ for all t , and $\lim_{t \rightarrow -\infty} \phi(t) = 0$, $\lim_{t \rightarrow +\infty} \phi(t)/t = 1$.

Proof. Maps $t \mapsto e^t$ and $x \mapsto \tanh x$ are C^∞ ; the product with t is smooth, hence $\phi \in C^\infty$. Since $|\tanh x| \leq 1$, we have $|\phi(t)| = |t| |\tanh(e^t)| \leq |t|$. As $t \rightarrow -\infty$, $u = e^t \rightarrow 0$ and $\tanh(u) = u + O(u^3)$, so $\phi(t) = t u + o(tu) \rightarrow 0$. As $t \rightarrow +\infty$, $\tanh(u) \rightarrow 1$, thus $\phi(t)/t \rightarrow 1$. \square

Lemma A.2 (Elementary bounds for the slope). For all $t \in \mathbb{R}$,

$$-|t|e^t \leq \phi'(t) \leq 1 + |t|e^t. \quad (12)$$

Consequently $\phi'(t) \rightarrow 0$ as $t \rightarrow -\infty$, and ϕ' is bounded on any compact interval.

Proof. Using $0 \leq \tanh(u) \leq 1$ and $0 \leq \operatorname{sech}^2(u) \leq 1$ in (11) gives $\phi'(t) \leq 1 + |t|u$ and $\phi'(t) \geq t u \geq -|t|u$ with $u = e^t$. Since $|t|e^t \rightarrow 0$ as $t \rightarrow -\infty$, the claims follow. \square

Proposition A.3 (Unique critical point and sign structure of ϕ'). There exists a unique $t_0 \in (-\infty, 0)$ such that $\phi'(t_0) = 0$, $\phi'(t) < 0$ for $t < t_0$, and $\phi'(t) > 0$ for $t > t_0$. In particular, TeLU has no flat dead zone: the derivative vanishes only at the isolated point t_0 .

Proof. Let $g(u) := \phi'(t)$ with $u = e^t$, i.e.

$$g(u) = \tanh(u) + (\ln u) u \operatorname{sech}^2(u), \quad u \in (0, \infty).$$

(1) If $u \geq 1$ then $\ln u \geq 0$, hence both terms are nonnegative and $g(u) > 0$; thus $\phi'(t) > 0$ for $t \geq 0$.

(2) For $u \downarrow 0$, expand $\tanh(u) = u + O(u^3)$ and $\operatorname{sech}^2(u) = 1 + O(u^2)$, so $g(u) = u + (\ln u) u + o(u) = u(1 + \ln u) + o(u) < 0$ for sufficiently small u . At $u = 1$, $g(1) = \tanh(1) > 0$; by continuity g has at least one zero in $(0, 1)$.

(3) To prove uniqueness on $(0, 1)$, differentiate:

$$\begin{aligned} g'(u) &= 2 \operatorname{sech}^2(u) + (\ln u) (\operatorname{sech}^2(u) - 2u \operatorname{sech}^2(u) \tanh(u)) \\ &= 2 \operatorname{sech}^2(u) + (\ln u) \operatorname{sech}^2(u) (1 - 2u \tanh(u)). \end{aligned}$$

Define $h(u) := u \operatorname{sech}^2(u)$. Then $h'(u) = \operatorname{sech}^2(u)(1 - 2u \tanh(u)) < 0$ for $u > 0$, so the factor of $\ln u$ above

is strictly decreasing and negative on $(0, 1)$. Hence $g'(u)$ changes sign at most once on $(0, 1)$, implying g crosses zero exactly once there. Translating back to $t = \ln u$, ϕ' has a single zero $t_0 \in (-\infty, 0)$ with the stated sign pattern. \square

Corollary A.4 (Monotonicity and near-identity in the active region). ϕ is strictly increasing on (t_0, ∞) and $\lim_{t \rightarrow +\infty} \phi'(t) = 1$; hence, the active region is near-linear and mimics identity for large positive input.

Proof. From Proposition A.3 we have $\phi'(t) > 0$ for $t > t_0$, giving strict monotonicity. Since $u = e^t \rightarrow \infty$ and $\tanh(u) \rightarrow 1$ while $\operatorname{sech}^2(u) \rightarrow 0$, we obtain $\phi'(t) \rightarrow 1$. \square

Proposition A.5 (Lipschitz continuity on compacts and curvature regularity). For any compact $I \subset \mathbb{R}$, ϕ is Lipschitz on I and ϕ'' is bounded on I . In particular, TeLU yields smooth slopes without the kink of ReLU at 0.

Proof. By Lemma A.2, ϕ' is bounded on I , so ϕ is Lipschitz on I . The explicit ϕ'' in (11) is continuous and bounded on compacts, hence curvature is controlled. \square

Summary. TeLU is C^∞ , strictly increasing for $t > t_0$, has a unique isolated critical point $t_0 < 0$, admits global usable bounds on ϕ' , and exhibits bounded curvature on compacts. These yield nonvanishing negative-side gradients, identity-like propagation on the positive side, and smooth training dynamics without extended dead zones.

A.2. From InfoNCE to Dispersive Loss

The InfoNCE objective encourages high similarity for a designated positive pair (z_i, z_i^+) while reducing similarity to all other samples. A common form is

$$\mathcal{L}_{\text{InfoNCE}} = -\log \left(\frac{\exp\left(-\frac{D(z_i, z_i^+)}{\tau}\right)}{\exp\left(-\frac{D(z_i, z_i^+)}{\tau}\right) + \sum_{j \neq i} \exp\left(-\frac{D(z_i, z_j)}{\tau}\right)} \right), \quad (13)$$

or equivalently

$$\mathcal{L}_{\text{InfoNCE}} = -\log \left(\frac{\exp\left(-\frac{D(z_i, z_i^+)}{\tau}\right)}{\sum_{j=1}^N \exp\left(-\frac{D(z_i, z_j)}{\tau}\right)} \right). \quad (14)$$

Here $D(\cdot, \cdot)$ denotes a dissimilarity measure and $\tau > 0$ is the temperature; the denominator pools both the positive and all negatives.

Using elementary log identities, InfoNCE can be rearranged into two parts:

$$\begin{aligned} \mathcal{L}_{\text{InfoNCE}} &= \frac{D(z_i, z_i^+)}{\tau} + \log \left(\exp\left(-\frac{D(z_i, z_i^+)}{\tau}\right) \right) \\ &\quad + \sum_{j \neq i} \exp\left(-\frac{D(z_i, z_j)}{\tau}\right). \end{aligned} \quad (15)$$

where the first term rewards the positive pair, and the second is a log-sum-exp normalization over the batch.

Motivated by the latter term, we retain only this normalization to promote dispersion without relying on explicit positives:

$$\mathcal{L}_{\text{Disp}} = \log \sum_{j=1}^N \exp\left(-\frac{D(z_i, z_j)}{\tau}\right). \quad (16)$$

For a usable batch objective, we average over anchors:

$$\mathcal{L}_{\text{Disp}} = \mathbb{E}_i \left[\log \sum_{j=1}^B \exp\left(-\frac{D(z_i, z_j)}{\tau}\right) \right], \quad (17)$$

which drives all representations in the batch to repel one another and mitigates representational collapse.

Dispersive Loss Variants **InfoNCE L2 Variant.** With squared Euclidean distance $D(h_i, h_j) = \|h_i - h_j\|_2^2$ and excluding $i = j$,

$$\mathcal{L}_{\text{disp}}^{\text{L2}} = \log \left(\frac{1}{B(B-1)} \sum_{i=1}^B \sum_{\substack{j=1 \\ j \neq i}}^B \exp\left(-\frac{\|h_i - h_j\|_2^2}{\tau}\right) \right). \quad (18)$$

InfoNCE Cosine Variant. Using cosine dissimilarity

$$D(h_i, h_j) = 1 - \frac{h_i^\top h_j}{\|h_i\|_2 \|h_j\|_2},$$

$$\mathcal{L}_{\text{disp}}^{\text{cos}} = \log \left(\frac{1}{B(B-1)} \sum_{i=1}^B \sum_{\substack{j=1 \\ j \neq i}}^B \exp\left(-\frac{1 - \frac{h_i^\top h_j}{\|h_i\|_2 \|h_j\|_2}}{\tau}\right) \right). \quad (19)$$

Hinge Loss Variant. Enforcing a margin $\epsilon > 0$ between representations:

$$\mathcal{L}_{\text{disp}}^{\text{hinge}} = \frac{1}{B(B-1)} \sum_{i=1}^B \sum_{\substack{j=1 \\ j \neq i}}^B \max\left(0, \epsilon - \|h_i - h_j\|_2\right)^2. \quad (20)$$

Covariance Off-Diagonal Penalty. Encouraging decorrelation across feature dimensions:

$$\mathcal{L}_{\text{disp}}^{\text{cov}} = \|C - \text{diag}(C)\|_F^2, \quad C = \frac{1}{B-1} \tilde{H}^\top \tilde{H}, \quad (21)$$

$$\tilde{H} = H - \mathbf{1} \bar{h}^\top, \quad \bar{h} = \frac{1}{B} \sum_{i=1}^B h_i.$$

Mathematical Properties of Dispersive Loss — Gradient Analysis. The gradient with respect to an anchor h_i takes a weighted repulsive form:

$$\frac{\partial \mathcal{L}_{\text{Disp}}}{\partial h_i} = \frac{1}{\tau} \sum_{j=1}^B w_{ij} \frac{\partial D(h_i, h_j)}{\partial h_i}, \quad (22)$$

$$w_{ij} = \frac{\exp\left(-\frac{D(h_i, h_j)}{\tau}\right)}{\sum_{\ell=1}^B \exp\left(-\frac{D(h_i, h_\ell)}{\tau}\right)}.$$

For $D(h_i, h_j) = \|h_i - h_j\|_2^2$ this reduces to

$$\frac{\partial \mathcal{L}_{\text{Disp}}}{\partial h_i} = \frac{2}{\tau} \sum_{j=1}^B w_{ij} (h_i - h_j), \quad (23)$$

so closer neighbors (with larger w_{ij}) exert stronger repulsion, naturally spreading batch representations.